Offshore Tower Shading Effects on In-Water Optical Measurements

GIUSEPPE ZIBORDI

Marine Environment Unit, Space Applications Institute, CEC/JRC, Ispra, Italy

JOHN PIERO DOYLE

CEC/JRC, Space Applications Institute, Marine Environment Unit, Ispra, Italy, and Department of Physics, Environmental Technology Centre, Imperial College, London, United Kingdom

STANFORD B. HOOKER

Laboratory for Hydrospheric Processes, NASA/GSFC, Greenbelt, Maryland

(Manuscript received 18 May 1998, in final form 9 December 1998)

ABSTRACT

A field campaign was performed to estimate the shading effect induced on in-water irradiance and radiance measurements taken in the immediate vicinity of the Acqua Alta Oceanographic Tower (AAOT), located in the northern Adriatic Sea, which is regularly used to support ocean color validation activities. Sequences of downwelling irradiance and upwelling radiance profiles were collected at varying distances from the tower to evaluate the shading effects during clear-sky conditions as a function of the deployment distance. The experimental data, as well as Monte Carlo simulations, indicate that the shading effect is negligible for both downwelling irradiances and upwelling radiances at deployment distances greater than 15 and 20 m, respectively. At closer distances, for example, at the 7.5-m deployment distance regularly used at the AAOT for the collection of underwater optical measurements, the shading effect is remarkable: both field and simulated data at a depth of 7 m and a wavelength of 443 nm show that, with a relatively low sun zenith angle of 22°, the shading effect is within 3% for downwelling irradiance and within 8% for upwelling radiance. Monte Carlo simulations at 443, 555, and 665 nm, computed at a depth of 0^- m and with values of seawater inherent optical properties representative of the AAOT site, are used to extend considerations on shading effects to measurements taken during different illumination conditions at the 7.5-m deployment distance. Simulations for ideal clear-sky conditions (i.e., in the absence of atmospheric aerosols) show that errors induced by AAOT perturbations significantly vary as a function of wavelength and sun zenith angle. The highest values are observed at 443 nm where, with the sun zenith angle ranging from 20° to 70°, errors vary from 2.4% to approximately 6.2% for downwelling irradiance and from a minimum of 3.0% (occurring at 30°) to almost 6.6% for upwelling radiance. Simulations also show that the shading error can be as high as approximately 20% for both irradiance and radiance measurements taken during overcast sky conditions.

1. Introduction

Marine bio-optical modeling, the validation of ocean color products, and the vicarious calibration of optical space sensors all require accurate in-water radiance and irradiance measurements. Light perturbation by the instrument itself, or by the large structures associated with the deployment of optical instruments (e.g., ships, offshore towers, moored buoys, etc.), can significantly reduce the accuracy of in-water radiometric measurements. Instrument self-shading, for example, can increase measurement uncertainty from a few percent to several tens percent as a function of wavelength, instrument radius, and illumination conditions (Gordon and Ding 1992). For such an effect, a correction scheme based on the absorption of seawater, instrument radius, sun zenith angle, and the ratio between diffuse and direct solar irradiances was proposed by Gordon and Ding (1992) and experimentally validated by Zibordi and Ferrari (1995).

In addition to instrument self-shading, various studies were performed to evaluate uncertainties induced in underwater optical measurements by large structures, such as ships. Investigations carried out by different authors (Gordon 1985; Voss et al. 1986; Helliwell et al. 1990; Weir et al. 1994; Saruya et al. 1996) indicate that radiance and irradiance measurement uncertainties increase substantially when the deployment distance of

Corresponding author address: Dr. Giuseppe Zibordi, SAI/TP 272, Joint Research Centre, Instituto Delle Appl. Spaziali, 21020 Ispra (VA), Italy.
E-mail: giuseppe.zibordi@jrc.it

the instrument from the stern of a ship is reduced. To minimize the ship-induced perturbation, a simple method was suggested by Mueller and Austin (1995) to estimate the minimum ship distance from the instrument deployment point as a function of the diffuse attenuation coefficient during clear-sky conditions.

The relatively infrequent use of offshore towers for in-water radiometric measurements is the reason for the dearth of studies on tower perturbation effects (Kearns et al. 1996). Consequently, minimization schemes for tower shading effects have not yet been developed, nor has it been assessed that the ship-based methods are applicable to a particular tower—the superstructure of a tower can be much different than a research vessel.

The need for quantifying the tower shading effects on optical measurements taken in the northern Adriatic Sea near the Acqua Alta Oceanographic Tower (AAOT) in support of calibration and validation activities (Zibordi et al. 1995) is the rationale for the present study. The major objectives of the work are the evaluation of (a) the experimental shading effects induced in in-water radiance and irradiance measurements by the tower, and (b) the capability of theoretically modeling the tower shading effects as a first step toward the development of an operational scheme for the correction of in-water optical measurements collected at the tower site.

2. Description of the experiment

An AAOT field experiment was designed to estimate shading effects on in-water radiometric data collected in close proximity to the tower. Sequential optical profiles taken with the Low Cost NASA Environmental Sampling System (LoCNESS) were used to determine the shading effects on downwelling irradiance, $E_d(\chi, z, \lambda, t)$, and upwelling radiance, $L_u(\chi, z, \lambda, t)$, where χ is the distance of the profiler from the tower, z is the water depth (or height above water), λ is the wavelength, and t is time. Concurrent with LoCNESS data, incident surface ($z = 0^+$ m) solar irradiance data (at $\chi = 0$ m), $E_s(0, 0^+, \lambda, t)$, were collected with a Multichannel Visible Detector System (MVDS). These incident irradiance measurements were used to normalize the underwater radiometric data to account for changes in the ambient light field during data collection. Underwater optical data were also taken with the Wire-Stabilized Profiling Environmental Radiometer (WiSPER) system, which is regularly used on the tower to collect radiance and irradiance profiles during measurement campaigns supporting ocean color calibration and validation activities.

a. The oceanographic tower

The AAOT is located in the northern Adriatic Sea (45.31°N, 12.51°E) approximately 15 km southeast of the city of Venice. The average water depth immediately below the tower is 17 m, and the composition of the nearby seafloor is primarily sand and silt. The tower was built in 1975 and is owned and operated by the Institute for the Study of Large Masses of the Italian *Consiglio Nazionale delle Ricerche* (National Research Council) in Venice. The tower is composed of four levels supported by four large pillars. Each level is approximately 7.2 m × 5.2 m in size with the exception of the lowest level, which is 5.2 m × 5.2 m.

The lowest tower level, about 4.5 m above the water, has an open grid deck and no facilities. The second level is approximately 7 m above the water and contains a workshop, two 12-kW diesel-powered electrical generators, a portable scientific laboratory, and storage spaces for a large complement of lead–acid batteries, fuel tanks, etc. At this level, a special open grid platform, 3.5 m wide, extends 6.5 m out over the sea toward the southeast. The platform provides mounting points for instruments to be deployed above, or into, the sea. The third deck contains the primary accommodation space. The fourth (uppermost) deck, at about 13 m above the water, contains a wind generator, solar panels, a variety of meteorological instruments, communications antennas, plus freshwater and seawater storage tanks.

b. The optical instruments

LoCNESS is a free-falling instrument based on the Sea-viewing Wide Field-of-view Sensor (SeaWiFS) Optical Profiling System (SeaOPS) composed of an above-water and in-water set of sensors, and several subsystems (Hooker and McClain 1999). The in-water optical sensors are a downward-looking radiance sensor, which measures $L_u(\chi, z, \lambda, t)$, and an upward-looking irradiance sensor, which measures $E_d(\chi, z, \lambda, t)$. The sensor used for upwelling radiance measurements is a Satlantic OCR-200 sensor (S/N 021), and the sensor used for downwelling irradiance measurements is an OCI-200 sensor (S/N 029). All of the sensors send their analog signals to an underwater data unit, a Satlantic DATA-100 (S/N 004), which digitizes the analog signals (16 bits) and converts the counts to RS-485 serial communications.

In the LoCNESS configuration, the DATA-100 and the two light sensors are connected in line using extension brackets with the OCR-200 at the nose (pointing downward to measure L_u) and the OCI-200 at the tail (pointing upward to measure E_d). The addition of weight to the nose bracket and buoyant (foam) fins to the tail bracket produces a balanced package that falls through the water column with minimum tilt (less than 2°). The power and telemetry cable to the profiler extends through the field of view (FOV) of the irradiance sensor, but the small diameter of the cable (7 mm) minimizes any negative effect on the measured light field.

The above-water part of SeaOPS, a Satlantic MVDS, measures $E_s(0, 0^+, \lambda, t)$. The MVDS unit (S/N 009) is composed of an OCI-200 irradiance sensor (S/N 030) packaged with a separate DATA-100 module that con-

TABLE 1. Nominal and actual center wavelengths [nm] of the optical radiometers used in the tower shading experiments. All instrument channels have 10-nm bandwidths.

Instrument	Sensor	S/N	412	443	490	510	555	665	683
LoCNESS	OCI-200	29	411.8	442.2	489.4	510.5	555.0	665.8	683.4
LoCNESS	OCR-200	21	412.0	442.6	489.6	510.7	555.3	665.7	683.4
WiSPER	OCI-200	71	411.3	442.9	490.2	510.1	554.8	665.6	683.6
WiSPER	OCR-200	46	412.3	442.8	490.5	510.8	554.9	665.8	683.9
MVDS	OCI-200	30	412.0	443.0	490.0	510.0	555.0	665.0	683.0

verts the analog output of the OCI-200 radiometer to RS-485 serial communications. For the shading experiments, the DATA-100 and OCI-200 units were mounted on a pole that was sited on the uppermost deck of the AAOT. The pole was long enough to ensure the tower superstructure did not shadow the irradiance sensor under almost all illumination conditions.

The RS-485 signals from the two DATA-100 units are combined in a Satlantic deck box, the PRO-DCU (S/N 023), and converted to RS-232 communications for computer logging. The deck box also provides the (computer controlled) power for all the sensors and is designed to avoid instrument damage due to improper power-up sequences over varying cable lengths. The RS-232 data were logged on two separate Macintosh PowerBook computers using software developed at the University of Miami Rosenstiel School for Marine and Atmospheric Science (RSMAS) and the SeaWiFS Project of the National Aeronautics and Space Administration's Goddard Space Flight Center (NASA/GSFC). The software controls the logging and display of the data streams as a function of the data collection activity being undertaken: dark data (caps on the radiometers), down cast, constant depth soak, up cast, etc. All of the telemetry channels are displayed in real time, and the operator can select from a variety of plotting options to visualize the data being collected.

The WiSPER system is permanently installed on the tower and is operated from the 6.5-m platform extension on the second level. WiSPER uses a custom-built profiling rig, and the positioning of the equipment on the rig was developed with a geometry that ensures all of the radiometers do not view any part of the mechanical supports. The radiometers are mounted on a 1-m extension boom, which places them approximately 7.5 m from the nearest tower leg. Two taut wires, anchored between the tower and the sea bottom, prevent the movement of the rig out of the vertical plane defined by the wires. The narrow geometry of the rig was designed to provide a minimal optical cross section. The FOV of the irradiance sensor is obstructed by the power and telemetry cable, as well as the stabilization wires, but all of these have very small cross sections that minimize the impact on measurements.

Careful attention was paid to the rigidity and stability of the rig, so tilt or roll sensors are not needed. WiSPER uses the same kind of optical sensors as LoCNESS: one OCI-200 (S/N 71) to measure $E_d(7.5, z, \lambda, t)$ and one OCR-200 (S/N 46) to measure $L_u(7.5, z, \lambda, t)$. The center wavelengths for the radiometers used with all of the optical systems are given in Table 1. The commonality in spectral properties for the optical devices used in the experiment was an important part of the equipment selection criteria. A special kind of DATA-100 (S/N 5) provides the analog-to-digital (A/D) and telemetry capability for the WiSPER instruments. The equipment is powered directly from 12-V lead–acid batteries, which are stored and kept charged on the tower. WiSPER is raised and lowered from the southeastern side of the tower. The typical lowering and raising speed of the winch used is approximately 0.1 m s^{-1}.

c. The experimental methodology

The experimental setup began with siting a black buoy approximately 30 m from the southern tower leg; the buoy was aligned perpendicularly to the southeastern side of the tower and displaced approximately 2 m to the side of the WiSPER instrument. Two pulleys were then attached—one to the buoy and the other to the tower—and a closed loop of line (60 m long) with marks on it every 2.5 m was run through the pulleys. A cable ring was linked to one of the cable marks that defined the current position of the profiler (the power and telemetry cable for the profiler passed through the ring). The ring and, thus, the profiler, was moved to a selected distance from the tower leg by pulling on the closed loop of line until the desired number of cable marks between the ring's position and the tower leg was achieved. A schematic of the experimental setup is given in Fig. 1.

LoCNESS is sufficiently easy to handle that one person can deploy it. Under normal circumstances, the handler keeps a few coils of the power and telemetry cable in the water, so the profiler can fall freely through the water column; once the desired depth has been reached, the cast is terminated and the profiler is pulled back to the surface (data are only logged during the down cast). For the tower deployments, the profiler was slowly lowered by hand to control the descent rate (approximately 0.4 m s^{-1}). A cable block, which could not pass through the cable ring, was used to prevent the profiler from going deeper than 15 m and accidentally impacting the seafloor (which might damage the radiometer in the nose of the instrument).

An experiment was defined as a sequence of profile

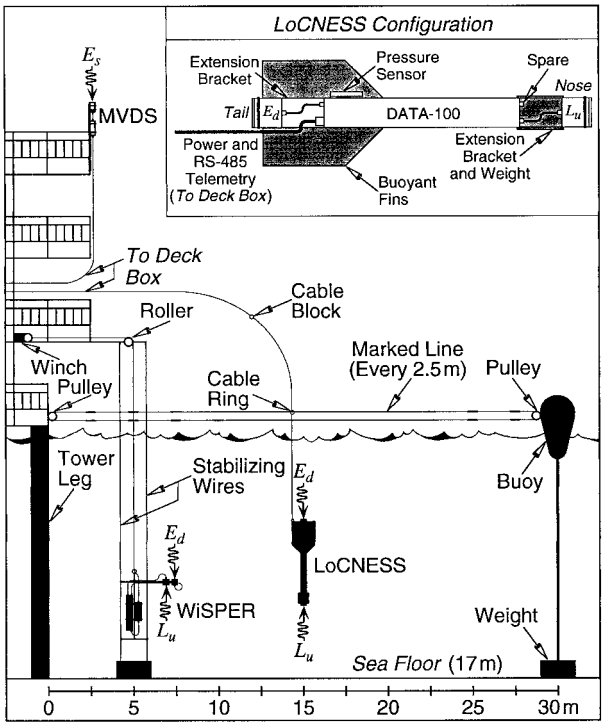

FIG. 1. A schematic of the technical setup at the AAOT showing the equipment and its relative positioning with respect to one another. The WiSPER instrumentation is shown in a slightly distorted view so all components are visible; in reality, the two radiometers and the two stabilizing wires are aligned in a plane perpendicular to the page, which means the light data are collected approximately 7.5 m away from the tower leg. Details of the LoCNESS instrument are shown in the inset panel.

deployments going away or toward the platform during a relatively short period of time (typically 20 min). For the tower deployments, 10 different experiments were conducted during almost clear-sky conditions: the first 9 with variable LoCNESS deployment distances (ranging from 2.5 to 22.5 m) with respect to the tower, and the last 1 with the deployment distance fixed at 7.5 m (the same distance the WiSPER measurements were made with respect to the tower).

At the end of the experiments, the LoCNESS and WiSPER optical sensors were intercompared by mounting them on the WiSPER frame in pairs: first, both OCR-200 sensors were used to collect coincident $L_u(7.5, z, \lambda, t)$ data, and then both OCI-200 sensors were used to collect $E_d(7.5, z, \lambda, t)$ coincident data.

3. Numerical modeling

The presence of a deployment structure at the measurement site introduces abrupt medium changes within a predominantly plane-parallel system, causing light field inhomogeneities in all three spatial dimensions. Consequently, the simulation of tower shading effects on in-water radiometric measurements requires a fully three-dimensional (3D) geometry description and radiative transfer modeling of the ocean–atmosphere system. In this fully 3D problem, the radiative transfer processes can be modeled with stochastic simulation methods to achieve a solution of the generalized radiative transfer equation (RTE). In particular, backward Monte Carlo (MC) techniques should be applied. These techniques, compared to forward MC techniques, produce much lower variances and concentrate only on significant contributions to the simulated light field.

a. Principles

The Photon-Transport (PHO-TRAN) MC code—jointly developed at the University of London, Imperial College of Science, Technology and Medicine (IC) together with the Joint Research Centre (JRC) of the Commission of the European Communities (CEC)—has been previously validated for the ocean–atmosphere system (Doyle and Rief 1998) and expanded to include backward MC techniques. This code has been employed in this work to assess the tower shading perturbations on in-water radiometric measurements. Algorithms, based on Case's reciprocity relationship (Case 1957) and Gordon's implementations (Gordon 1985), were introduced in the PHO-TRAN backward MC code to compute radiances and irradiances at a specific point in the modeled system.

Within the simulations, the ocean–atmosphere system is modeled on a 3D grid. The grid delimits the largest macroscopic volumes (cells) containing medium of uniform optical properties. In each cell of the grid, the optically active components (air or water molecules, hydrosols, aerosols, etc.) are specified, and their spectral inherent optical properties (IOPs) are assigned (e.g., the beam attenuation coefficient c, the single scattering albedo ω_0, and the scattering phase function P). Cell boundaries are spectrally characterized by transmittance and reflectance, and by the associated transmission and reflection angular distribution functions (ADFs). Specific ADFs are also defined both for the source angular emission and for the detector angular collection. The air and water refractive indices are assigned to the atmosphere and ocean, respectively.

Photons detected by a radiometer are a fraction of those emitted by the sun and reach the sensor after absorption, scattering, reflection, and refraction processes in the ocean–atmosphere system. The properties of physical processes characterizing the propagation of photons are time reversal invariant; hence the inverse course of events can be applied in simulations. This principle is the basis for the backward MC technique. Random-walk photon trajectory sampling is performed the same in backward MC simulations, as in forward MC simulations, but contributions to the detected signal are deterministically computed ensuring high computational efficiency.

In the backward MC scheme, photons, initially having unitary statistical weight, are released from the detector

within its FOV according to the predefined ADF. A free-flight optical distance to the next collision point is sampled (Lux and Koblinger 1991), possible cell-boundary crossing processes are considered to define flight direction modifications, and finally, photon trajectory is computed taking into account possible changes in IOP values along the trajectory. At the collision point (defined as the point where the sampled optical distance is exhausted), a scatterer is sampled; photon survival probability, given by ω_0, is computed (accounting for absorption a); and the flight direction of the surviving photon is determined by retrieving the scattering angle from a random sampling of P. The latter is adequately modeled into an equal probability interval table (Lux and Koblinger 1991).

The probability of a backtracked photon propagating toward the sun is virtually zero; therefore, at collision and boundary crossing points, photon contributions to the detected signal are deterministically computed. This is done by calculating the probability that a photon scatters in directions leading to the sun and evaluating the associated weight reduction, given both by attenuation along the traveled path and by possible absorption at interface transmission. If this virtual photon encounters a purely absorbing medium (i.e., the tower structure), its contribution to the detected signal is zero.

By tracking so-called twin photons, one interacting with the tower and the other not, a correlated sampling scheme (Spanier and Gelbard 1969) is produced, which minimizes the score variance of differences between tower-perturbed and unperturbed signals. The number of initiated twin photons defines the estimated statistical relative error on simulated data.

b. Simulations

The simulation frame consisted of one large 3D box that enclosed the grid defining the geometrical features of the problem. The atmosphere, the ocean, and the boundaries (top of the atmosphere, sea surface, and seafloor) were modeled as horizontally plane-parallel. This plane-parallel symmetry was broken by introducing, at a specific location within the reference frame, a geometrical object schematically representing the tower with completely absorbing surfaces. The reference system for the simulation frame used Cartesian orthonormal coordinates (x, y, z), centered at a tower leg. Figure 2 shows the schematic of the tower structure and the relevant 3D features introduced in the geometry description of the PHO-TRAN code. It is important to note the presence of the platform, which is used for routine deployment of the optical instruments and stretches out from the main structure of the tower. Moreover, in this section, the modeling is described from the forward MC perspective, even though backward MC is the actual technique adopted in tracking and tallying photons through the modeled ocean–atmosphere system.

The direct source (i.e., the source in a forward MC scheme perspective—the sun) was represented by a parallel beam of photons uniformly incident at the top of the atmosphere. The ADF for the source emission was formulated by a δ Dirac centered on the sun zenith θ_0 and sun azimuth ϕ_0 angles. Radiometers, located at specific points in the reference frame, were described by their FOV and the associated photon-collection ADF. Radiances were simulated assuming an in-water 20° FOV (as per the OCR-200 specifications) with a unitary collection ADF; irradiances were simulated assuming a 2π sr FOV with a cosine collection ADF. Downwelling irradiances and upwelling radiances were simulated for intercomparison with field data taken at the tower site. Simulations were performed at different wavelengths (coinciding with the center wavelengths of the radiometers), at different depths, and at different distances from the tower legs.

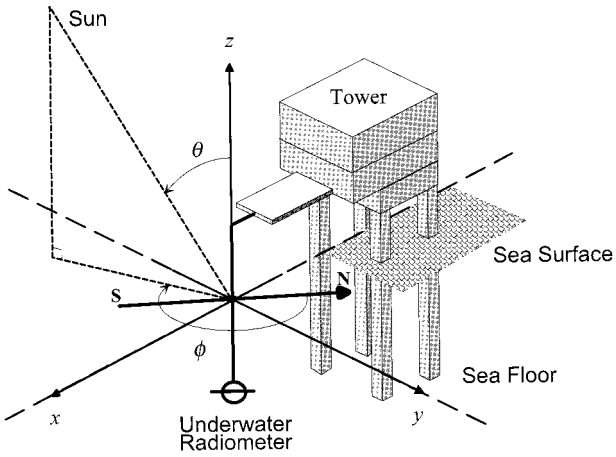

FIG. 2. Schematic of the tower as defined in the PHO-TRAN Monte Carlo code. The south–north direction is rotated 135° with respect to the positive x axis. The surfaces obstructing photons are shown in gray.

The atmosphere was modeled by 50 plane-parallel and homogeneous layers 1 km thick, and was stratified according to the Elterman (1968) atmospheric model. The individual ozone, molecular, and aerosol relative concentration profiles were weighted by the respective optical thickness as derived climatologically for ozone (Vigroux 1953; Robinson 1966; and Leckner 1978), theoretically for molecules (Frölich and Shaw 1980; Young 1980), and experimentally for aerosols. In particular, the aerosol optical thicknesses τ_A at the wavelengths of interest were obtained by applying the Ångström law (Ångström 1961) to measurements taken during the experiment at 440, 500, and 670 nm with a sun photometer (CIMEL CE-318). The optical thicknesses of the atmospheric components were then used to compute c and ω_0 for each atmospheric layer. The Rayleigh molecular scattering phase function and the Gordon and Castaño (1987) marine aerosol scattering phase function were adopted.

The sea surface was assumed flat, and the incident

light was reflected and refracted according to the Fresnel and Snell laws, respectively. The extraterrestrial solar irradiance was assumed to be a constant in the computations (1.0 W m^{-2} nm^{-1}). An absolute quantity is not needed, because the field data and simulated data intercomparison relies on radiance or irradiance ratios to derive tower shading perturbations. The ADF for seafloor reflection was assumed to be Lambertian. The seafloor reflectance R_b was derived by performing the ratio of upwelling to downwelling irradiance, as provided by ad hoc measurements taken close to the seafloor.

The water column was modeled by N plane-parallel, homogeneous layers (where N is the number of significant stratification layers chosen for the simulations). Profiles of c and a, taken with an attenuation absorption meter (WET-LABS AC9) operated during the experiment, were used to define $\omega_0 = (c - a)/c$ for each water layer. The Rayleigh and Gordon KA (Gordon et al. 1975) scattering phase functions were used for water molecules and particulate matter, respectively.

4. Comparison of the in situ and numerical results

The LoCNESS radiometers sample the water column at slightly different depths and times. To account for temporal changes in the ambient light field, the in-water optical measurements were normalized by the solar irradiance measured on the tower; that is, the E_d and L_u values for a given profile (indicated by χ) at a particular depth, wavelength, and time were divided by the corresponding incident solar irradiance at the same time:

$$nE_d(\chi, z, \lambda, t) = \frac{E_d(\chi, z, \lambda, t)}{E_s(0, 0^+, \lambda, t)} \quad \text{[dimensionless]} \quad (1)$$

and

$$nL_u(\chi, z, \lambda, t) = \frac{L_u(\chi, z, \lambda, t)}{E_s(0, 0^+, \lambda, t)} \quad [\text{sr}^{-1}]. \quad (2)$$

The depth coregistration of optical data was achieved by data binning. The $nE_d(\chi, z, \lambda, t)$ and $nL_u(\chi, z, \lambda, t)$ profile data were binned at depths z_i using depth intervals of 0.5 m (ranging from $z_i + 0.25$ m to $z_i - 0.25$ m) resulting in $nE_d(\chi, z_i, \lambda, t_i)$ and $nL_u(\chi, z_i, \lambda, t_i)$ values, where t_i is the average time for each binning interval associated with depth z_i.

The analysis of $nE_d(\chi, z_i, \lambda, t_i)$ and $nL_u(\chi, z_i, \lambda, t_i)$ has shown that for several experiments the shading effects were masked out by the presence of mucilage (Degobbis et al. 1995; Molin et al. 1992), which was clearly observed during many of the optical deployments. The mucilage, in the form of highly scattering, inhomogeneous, thick layers, of gelatinous aggregates (Berthon et al. 1999, submitted to *Limnol. Oceanogr.*), induces spatial and temporal variability in the in-water light field. This is clearly shown in Fig. 3 for the LoCNESS $nE_d(\chi, z_i, \lambda, t_i)$ and $nL_u(\chi, z_i, \lambda, t_i)$ profiles, which were obtained in almost ideal conditions with no evidence of mucilage (Fig. 3a) and in the presence of mucilage (Fig. 3b). The data analysis is restricted to 443, 555, and 665 nm, assumed as representative wavelengths of the visible spectrum.

The multiple profiles taken in the absence of mucilage and at a variety of distances from the tower (Fig. 3a) show almost regular and correlated variations; in comparison, the multiple profiles taken in the presence of mucilage (Fig. 3b) show irregular variations with respect to both distance and depth. A careful examination of the $nE_d(\chi, z_i, \lambda, t_i)$ values indicates higher noise in the surface data between 0- and 4-m depth for the former than for the latter. This is a consequence of the more pronounced wave effects induced in Fig. 3a profiles by a sea state of about 2 (code ''S'' units), which was higher than the sea state of approximately 1 observed during the collection of the Fig. 3b profiles. Further examination of $nL_u(\chi, z_i, \lambda, t_i)$ in Fig. 3a clearly shows the bottom effects that, becoming more pronounced on depth increase, induce a change in the slope of profiles. This change is not appreciable at 443 nm but appears significant at 555 nm and 665 nm in agreement with the relatively low R_b at 443 nm, and the much higher R_b values at 555 nm and 665 nm (see Table 2). Different from Fig. 3a, the bottom effects on $nL_u(\chi, z_i, \lambda, t_i)$ profiles shown in Fig. 3b are masked out by the scattering of mucilage layers.

For the shading analysis presented below, only the data in Fig. 3a (i.e., not contaminated by mucilage) were used.

The percent change between radiometric quantities at different deployment distances away from the tower are discerned by choosing one deployment point as an origin, χ_o, and then dividing the depth bins at all deployment points by the appropriate depth bin at the origin. Therefore, $nE_d(\chi, z_i, \lambda, t_i)$ and $nL_u(\chi, z_i, \lambda, t_i)$ space series were renormalized by the measurement taken at the origin point, $nE_d(\chi_o, z_i, \lambda, t_i)$, and $nL_u(\chi_o, z_i, \lambda, t_i)$, respectively, obtaining the following quantities:

$$nE'_d(\chi, z_i, \lambda, t_i) = \frac{nE_d(\chi, z_i, \lambda, t_i)}{nE_d(\chi_o, z_i, \lambda, t_i)} \quad \text{[dimensionless]} \quad (3)$$

and

$$nL'_u(\chi, z_i, \lambda, t_i) = \frac{nL_u(\chi, z_i, \lambda, t_i)}{nL_u(\chi_o, z_i, \lambda, t_i)} \quad \text{[dimensionless]}. \quad (4)$$

For the following analyses, 22.5 m was chosen as the

TABLE 2. Truth data used for theoretical computations given in Fig. 4 at different nominal center wavelengths [nm].

Parameter	Depth	Units	443	555	665
τ_A	—	—	0.051	0.039	0.031
R_b	—	%	1.8	6.1	26.6
c	0–11.5 m	m^{-1}	0.556	0.490	0.790
ω_0	0–11.5 m	—	0.858	0.831	0.426
c	11.5–17.5 m	m^{-1}	1.050	0.933	1.188
ω_0	11.5–17.5 m	—	0.799	0.870	0.592

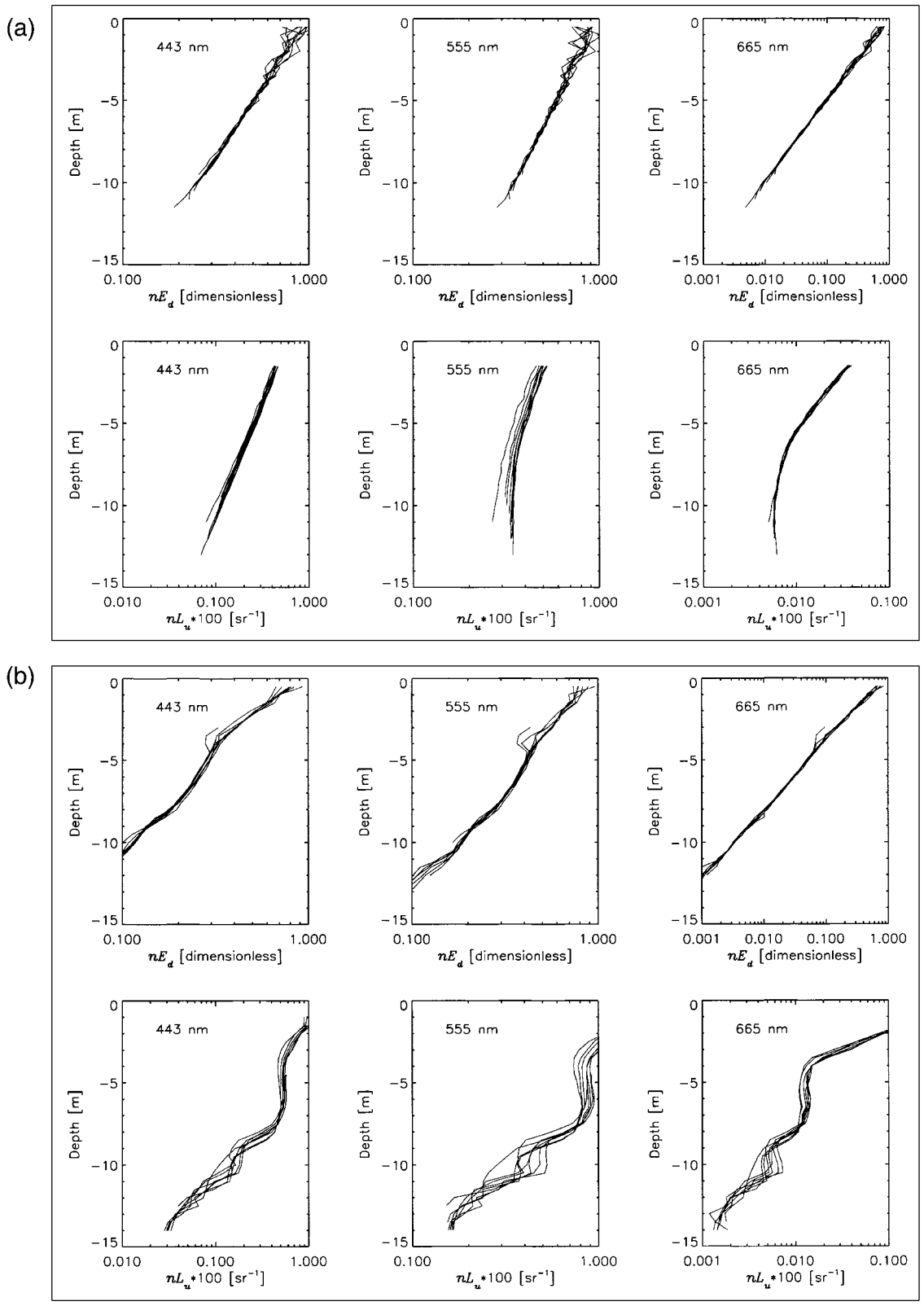

FIG. 3. LoCNESS profiles of nE_d and nL_u data in the first six panels (a) ideal conditions, and in the last six panels (b) in the presence of mucilage. Profiles are given at 443-, 555-, and 665-nm center wavelengths and for different distances from the tower. The profiles in (a) were taken with θ_0 between 22° and 23° and ϕ_0 between 182° and 194°; the profiles in (b) were taken with θ_0 between 43° and 47° and ϕ_0 between 101° and 105°.

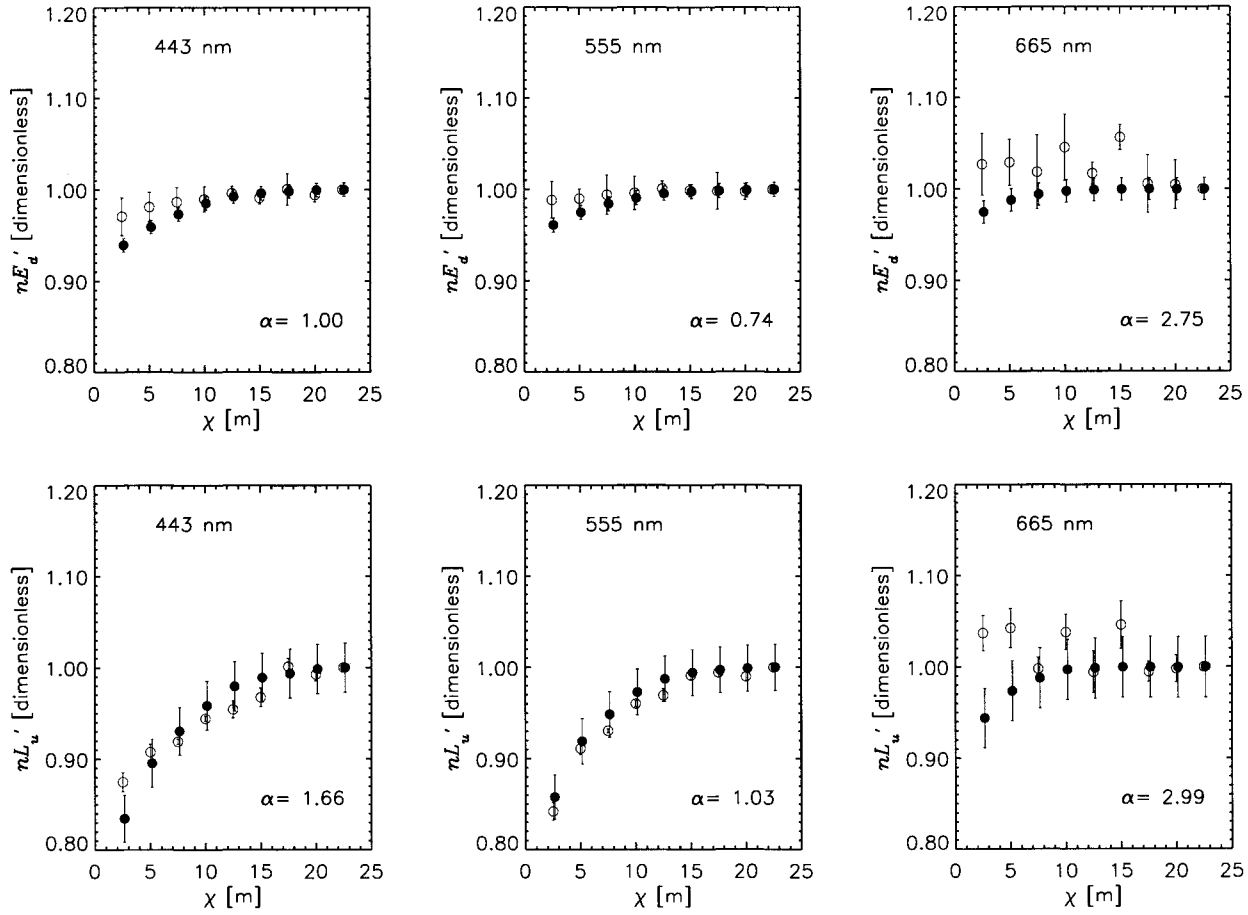

FIG. 4. Irradiance and radiance relative variations nE'_d and nL'_u, respectively, as a function of distance from the tower, as obtained from the profiles given in Fig. 3a. Data are given at a depth of 7 m and at the nominal center wavelengths 443, 555, and 665 nm. The open circles indicate experimental data, while the solid circles indicate simulated data assuming $\theta_0 = 23°$ and $\phi_0 = 190°$. The vertical bars on the open circles indicate standard deviation for experimental data, while vertical bars on solid circles show the confidence limits for the simulated data. To distinguish between experimental and simulated error bars, the solid circles have been shifted by 0.1 m along the χ axis.

origin, assuming that for the given environmental conditions the tower shading effects are negligible at this distance (so the nE'_d and nL'_u values at $\chi = 22.5$ m are equal to 1.0).

To minimize wave effects—which can induce noise of the order of several percent in surface values even after fitting of profile data (Mueller and Austin 1995)—as well as to avoid intervals close to the bottom where data were not available, the analysis of nE'_d and nL'_u has been carried out using depth bins at intermediate depths.

A plot of nE'_d and nL'_u experimental data (empty circles) is given in Fig. 4 as a function of χ. These values, given at $z_i = 7$ m, result from the averaging of the five depth bins between $z_i = 6$ m and $z_i = 8$ m. The averaging is applied to smooth out the relevant wave noise still present at several meters depth. The error bars on symbols associated with the experimental data represent the standard deviation of the plotted mean values. PHOTRAN simulations at $z_i = 7$ m are also shown in Fig. 4 as solid circles. The related error bars represent the confidence limits resulting from the precision spread produced by the estimated standard deviation on the mean simulated signal, which was generated with 100 000 initiated and tracked photons. The simulated data were computed using the parameters in Table 2 and were obtained from field measurements (i.e., τ_A, R_b, plus c and ω_0). Values of c and ω_0 are given for the 0–11.5-m and 11.5–17.5-m layers, as identified and characterized by in situ profiles of a and c.

The nE'_d data in Fig. 4 (top three panels) show that a slight trend characterizes the downwelling irradiance changes as a function of χ, with the exception of experimental data at 665 nm. Simulated data show that at $\chi = 7.5$ m (i.e., at the location of the WiSPER radiometers) irradiance percentage changes—with respect to values at $\chi = 22.5$ m—are less than 3%, 2%, and 1% at 443, 555, and 665 nm, respectively. The nL'_u data in Fig. 4 (bottom three panels) show that, again with the exception of experimental data at 665 nm, the upwelling radiance has a pronounced dependence on χ.

Simulated data show that at $\chi = 7.5$ m, radiance percentage changes are less than 7%, 5%, and 2% at 443, 555, and 665 nm, respectively. The nE'_d and nL'_u experimental data at 665 nm do not exhibit any evident dependence on χ and they are, as expected, very noisy; their high standard deviation can be mainly attributed to wave effects acting on the direct sun irradiance transmitted across the sea surface. This direct component represents an increasingly larger percentage of the total signal at longer wavelengths.

Intercomparison between the simulated and experimental data given in Fig. 4 is quantified through mean percentage differences, α, which is defined as

$$\alpha = \frac{1}{M}\sum_{j=1}^{M} 2\frac{|\tilde{V}_j - \overline{V}_j|}{\tilde{V}_j + \overline{V}_j} \times 100 \quad [\%], \tag{5}$$

where $\tilde{V}_j$ is the measured radiometric value (nE'_d or nL'_u) for the jth profile taken at distance χ, $\overline{V}_j$ is the corresponding simulated value, and M is the number of profiles considered. The computed α's range from approximately 0.8% to 3.0%, exhibiting the highest values at 665 nm. These α's, biased by the nE'_d (or nL'_u) measured and computed at $\chi > 10$ m (which are characterized by low shading effects), do not, however, ensure a complete assessment of the intercomparisons proposed in Fig. 4. Thus, a more extensive evaluation is drawn from the observation of simulated and measured data as a function of χ.

A remarkable agreement between simulated and experimental data is observed for nL'_u at 443 and 555 nm: the experimental data are generally within the confidence limits of the simulated data. On the contrary, a slightly different trend characterizes experimental and simulated values of nE'_d at 443 and 555 nm. In fact, for $\chi < 10$ m, the experimental data show systematically higher values than those of simulated data. This is probably because of the approximations introduced in the description of the AAOT within the PHO-TRAN code: a simplified geometry and the assumption of *completely absorbing* surfaces (needed by the correlated sampling scheme used in the code). The latter assumption is likely to produce an overestimate of the shading effects. These overestimates are expected to be more pronounced in nE'_d rather than in nL'_u because E_d measurements (taken with the tower projected into the field of view of the radiometer) are more sensitive than L_u measurements to light reflected by the tower surfaces. It is also possible that radiance and irradiance contributions, due to reflectance of the AAOT surfaces, are the sources of the nE'_d and nL'_u experimental values higher than 1.0, as observed at 665 nm for $\chi \leq 15$ m.

5. Discussion

In the following sections, accounting for the satisfactory results obtained from the intercomparison between simulated and experimental data, a theoretical analysis of the tower shading effects is presented as a function of typical environmental conditions at the AAOT measurement site. In addition, an intercomparison of LoCNESS and WiSPER data is briefly presented to demonstrate the equivalence of the tower shading effects on measurements taken with the two devices working in identical geometric and environmental conditions.

TABLE 3. Typical IOPs used for the computations given in Fig. 5 at different wavelengths [nm].

Parameter	Units	443	555	665
c	m^{-1}	0.939	0.744	0.987
ω_0	—	0.837	0.860	0.534

a. Theoretical analysis of the tower shading effects

The intercomparison between experimental and PHO-TRAN simulated data has shown mean percentage differences α of 1.0% and 0.8% for irradiance and of 1.7% and 1.0% for radiance at 443 and 555 nm, respectively. Although code assessment with field data is restricted to a single experiment (because of the difficulty in performing the needed measurements under the required environmental conditions), the result of the intercomparison suggests that PHO-TRAN is a viable code for the evaluation of the AAOT shading errors on underwater radiance and irradiance collected at various geometric and physical conditions.

By defining the tower shading percentage error ε_V as

$$\varepsilon_V = \frac{\hat{V} - \tilde{V}}{\hat{V}} \times 100 \quad [\%], \tag{6}$$

where $\hat{V}$ is the actual (or true) value and $\tilde{V}$ is the measured (shading contaminated) value for radiance or irradiance, a theoretical sensitivity analysis on AAOT shading errors has been carried out. PHO-TRAN computations have been performed assuming the typical values for seawater IOPs, as given in Table 3, and two extreme illumination conditions: overcast sky (i.e., producing a completely diffuse illumination) and ideal clear sky (i.e., $\tau_A = 0$) with varying θ_0, $\phi_0 = 180°$, and $\chi = 7.5$ m. The value for χ was chosen to ensure exploration of the AAOT shading effects at the location of the WiSPER radiometers; the value of ϕ_0 was chosen to simulate the mean measurement conditions in which WiSPER is deployed from the sunny side of the tower (see Fig. 2). Table 3 data for c and ω_0 were obtained from average values of a (obtained from in vivo absorption measurements) and subsurface water reflectance, R, collected at the tower site over a 2-yr period. Values for R and a were used to derive the scattering coefficient b, using Kirk's (1994) experimental relationship

$$b = a\left(\frac{103R}{1 - R}\right) \quad [m^{-1}]. \tag{7}$$

TABLE 4. Computed shading errors on subsurface downwelling irradiance E_d (7.5, 0^-, λ) and upwelling radiance L_u (7.5, 0^-, λ) (the dependence on the time parameter t is not necessary here) for a diffuse light source assuming *typical* values of inherent optical properties, at different wavelengths [nm]. Confidence intervals are given in parentheses.

Parameter	Units	443	555	665
ϵ_{E_d}	%	19.8 (±0.2)	19.9 (±0.2)	20.1 (±0.2)
ϵ_{L_u}	%	19.5 (±0.1)	18.5 (±0.1)	19.8 (±0.1)

From the measured a and the estimated b, c and ω_0 were computed according to $c = a + b$ and $\omega_0 = b/c$; this approach was adopted since a and c data from the AC-9 were not available during the 2-yr sampling period.

Simulated downwelling irradiance errors, ε_{E_d}, and upwelling radiance errors, ε_{L_u}, are summarized in Table 4 for overcast sky conditions and in Fig. 5 for clear sky conditions at $z = 0^-$ m and 443, 555, and 665 nm.

Analysis of the data in Table 4 shows values almost independent of wavelength for both ε_{E_d} and ε_{L_u}. In fact, by assuming that for an overcast sky most of the perturbation effects are induced by interaction of the (diffuse) irradiance field with the above-water structure of the tower, the shading error becomes closely proportional to the perturbed above-water irradiance. Consequently, ε_{E_d} values—and analogously ε_{L_u} values—exhibit no significant dependence on λ.

Values of ε_{E_d} and ε_{L_u} in Fig. 5 show a strong dependence on θ_0 and λ. The ε_{E_d} data show values increasing with θ_0 increase, while the ε_{L_u} data show a more complex dependence on θ_0 exhibiting minimums close to 30° and 40° at 443 nm and 555 nm, respectively. The dependence on θ_0 can be explained by the different perturbations induced by the AAOT on the nearby light field. Under fully diffuse illumination, the diffuse sky irradiance E_{sky} is solely responsible for the in-water light field and the tower shading is uniformly cast in all directions. During clear-sky conditions, when both the E_{sky} and the direct sun irradiance E_{sun} contribute to the in-water light field, the perturbation associated with E_{sky} adds to the perturbation associated with E_{sun}. The latter perturbation results in a pronounced tower shadow projected in the direction opposite to the sun, which is also opposite to the measurement side of the tower. Then, during clear-sky conditions, excluding cases characterized by very low values of θ_0, E_{sun} creates perturbations that are confined at some distance from the measurement point. These perturbations induce shading errors, which decrease with increasing θ_0, as shown in Fig. 6 (the ε_{E_d} and ε_{L_u} values shown in Fig. 6 have been computed analogously to those proposed in Fig. 5, but assuming no atmosphere). These errors add to those induced by E_{sky}, which increase as θ_0 increases. Consequently, the resulting error varies significantly both with θ_0 and with the ratio E_{sky}:E_{sun}, exhibiting the trends shown in Fig. 5 for ε_{E_d} and ε_{L_u}. The ε_{E_d} values shown in Fig. 6, contrary to the ε_{L_u} values, should be virtually zero at 0^- m. However, for computational needs, a tiny depth of 1 mm is assigned to the E_d sensor. This depth induces the observed nonzero ε_{E_d} at 0^- m, which in any case has little weight on the ε_{E_d} values of Fig. 5.

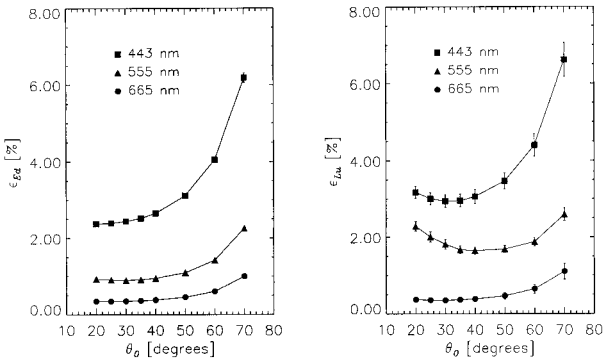

FIG. 5. Computed shading errors ε_{E_d} and ε_{L_u} at a depth of 0^- m and 7.5 m distance from the tower as a function of θ_0, assuming $\phi_0 = 180°$ and ideal clear-sky condition. The vertical bars show the confidence limits for the simulated data.

b. *Intercomparison of WiSPER and LoCNESS data*

In order to demonstrate that the tower shading effects estimated using the LoCNESS profiler were consistent with WiSPER data (i.e., that radiometric measurements performed with LoCNESS and WiSPER were equally influenced by tower shading), sample profiles obtained simultaneously with the two systems operating at 7.5 m from the tower legs were intercompared.

The first step in the radiometric intercomparison was the intercalibration of the OCI-200 and OCR-200 instruments used with LoCNESS and WiSPER. Intercalibration factors were obtained using the profiles collected with the two radiance sensors, and then with the two irradiance sensors, installed at the same time on the WiSPER system. By assuming that the active radiometers were measuring the same light field, the intercal-

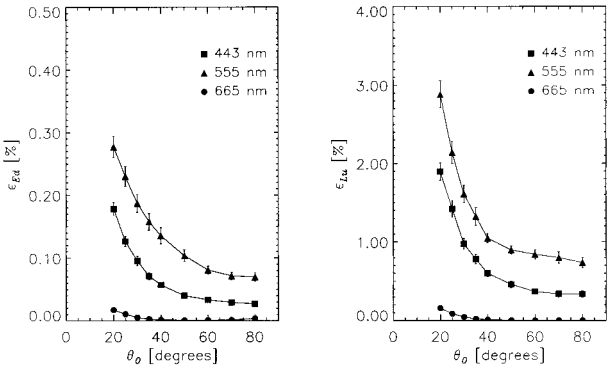

FIG. 6. Computed shading errors ε_{E_d} and ε_{L_u} at a depth of 0^- m and 7.5 m distance from the tower as a function of θ_0, assuming $\phi_0 = 180°$ and no atmosphere. The vertical bars show the confidence limits for the simulated data.

ibration factors for the two OCR-200 sensors were obtained by forming the ratio between the two radiance profiles on a depth-binned basis; the intercalibration factors for the two OCI-200 sensors were obtained in an analogous fashion using the irradiance profile data. The derived calibration factors were applied to LoCNESS and WiSPER data for intercomparing E_d and L_u obtained with the two profiling systems operating at the same time at 7.5 m from the tower. Average percentage differences obtained from binned LoCNESS and WiSPER profile data are within 2% for irradiances and within 3% for radiances. The differences are explained by the presence of mucilage during the intercomparison casts. A better agreement is expected under *normal* measurement conditions, that is, in the absence of inhomogeneous scattering layers in the water column. Thus, it is assumed that any conclusion on tower shading effects achieved from the analysis of LoCNESS data is also correct for WiSPER data.

6. Conclusions

The sequences of irradiance and radiance profiles taken at varying distances from the AAOT to quantify the tower shading perturbations on underwater optical measurements have shown very appreciable shading effects at 443 and 555 nm, while reflections from the tower surfaces and noise induced by surface waves have largely masked out the shading effects at 665 nm. At the 7.5-m deployment distance regularly used on the AAOT for the collection of underwater optical measurements, the shading effect at a depth of 7 m and at a wavelength of 443 nm with a relatively low sun zenith angle of 22° has been quantified within 3% for downwelling irradiance and within 8% for upwelling radiance. For the specific field experiment, the shading effects have been shown to be negligible for both E_d and L_u at deployment distances greater than 15 and 20 m, respectively.

The PHO-TRAN code, assessed with the experimental data, was used to extend the analysis to AAOT shading effects for measurements taken at a depth of 0^- m and at a deployment distance of 7.5 m during different illumination conditions. Simulations, performed assuming seawater IOPs representative of the AAOT site, showed that the measurement conditions minimizing the tower perturbations are those performed on very clear sky conditions with θ_0 between 20° and 60°. In such a case, for the simulated conditions, the error is lower than approximately 4.0%, 1.5%, and 0.5% for irradiance and lower than approximately 4.5%, 2.5%, and 0.6% for radiance at 443, 555, and 665 nm, respectively.

Simulations have also shown, however, that the shading error can be as high as approximately 20% and almost independent of wavelength for both irradiance and radiance measurements taken during overcast sky conditions. Then, actual AAOT shading errors at a depth of 0^- m and 7.5 m from the tower (for the average seawater IOPs characterizing the site) will result in a combination of the case studies presented above. Because of this, given that the SeaWiFS Project requires radiometric field data with a measurement uncertainty below 5% (Hooker and Esaias 1993), a correction scheme to minimize the tower shading effects in optical measurements taken near the tower is needed if the data are to be used for ocean color validation activities.

This study suggests the development of an operational correction scheme based on lookup tables of AAOT shading correction factors, computed with the PHO-TRAN code for a wide range of measurement conditions identified by a minimum set of parameters collected simultaneously as the in-water optical profiles. The adoption of lookup tables, making the correction of AAOT shading effects independent from the relatively high MC computational time required by PHO-TRAN, would make possible real-time correction of the optical in-water measurements.

Acknowledgments. The authors acknowledge Dirk van der Linde for his support in preparing the tower shading experiment and during its execution, Jean-François Berthon for providing the AC-9 processed data and contributing to helpful discussions, Stephane Maritorena for providing comments on an early draft of the paper, and Elaine Firestone for the editorial revision of the manuscript. The authors would also like to thank Luigi Alberotanza for ensuring the use of the tower and Pierluigi Cova, Armando Penzo, and Narciso Zennaro for the logistic support provided during the field work.

APPENDIX A

Symbols

Symbol	Units	Definition
χ	m	Distance from tower leg, perpendicularly from tower deployment side
z	m	Geometric depth, measured positive downward
λ	nm	Wavelength
t	s	Time
E_d	W m^{-2} nm^{-1}	Downwelling irradiance

L_u	W m^{-2} sr^{-1} nm^{-1}	Upwelling radiance
$E_d(\chi, z, \lambda, t)$	W m^{-2} nm^{-1}	Downwelling irradiance, depth profiled spectrally, at χ and time t
$L_u(\chi, z, \lambda, t)$	W m^{-2} sr^{-1} nm^{-1}	Upwelling radiance, depth profiled spectrally, at χ and time t
$E_s(0, 0^+, \lambda, t)$	W m^{-2} nm^{-1}	Above water atmospheric irradiance, spectrally measured at the tower and at time t
a	m^{-1}	Total absorption coefficient
b	m^{-1}	Total scattering coefficient
c	m^{-1}	Total beam-attenuation coefficient
P	sr^{-1}	Scattering phase function
ω_0	—	Single scattering albedo (scattering-to-attenuation ratio: $\omega_0 \equiv b/c$)
x, y, z	m	Cartesian coordinate axis
δ	—	Dirac δ
τ_A	—	Aerosol optical thickness
R_b	—	Seafloor irradiance reflectance
R	—	In-water irradiance reflectance
$nE_d(\chi, z, \lambda, t)$	—	$E_d(\chi, z, \lambda, t)$ values normalized by $E_s(0, 0^+, \lambda, t)$
$nL_u(\chi, z, \lambda, t)$	sr^{-1}	$L_u(\chi, z, \lambda, t)$ values normalized by $E_s(0, 0^+, \lambda, t)$
z_i	m	Intermediate depth of the ith interval at which profile binning is performed
t_i	s	Average time the ith interval at which binning of profiles is performed
$nE_d(\chi, z_i, \lambda, t_i)$	—	Time and depth-binned normalized downwelling irradiance
$nL_u(\chi, z_i, \lambda, t_i)$	sr^{-1}	Time and depth-binned normalized upwelling radiance
χ_o	m	Data normalizing distance (22.5 m) from tower leg
$nE'_d(\chi, z_i, \lambda, t_i)$	—	$nE_d(\chi, z_i, \lambda, t_i)$ values normalized by $nE_d(\chi_o, z_i, \lambda, t_i)$
$nL'_u(\chi, z_i, \lambda, t_i)$	—	$nL_u(\chi, z_i, \lambda, t_i)$ values normalized by $nL_u(\chi_o, z_i, \lambda, t_i)$
α	—	Mean percentage difference between simulated and experimental data
M	—	Number of profiles used to evaluate α
$\tilde{V}_{(j)}$	Counts	Measured radiometric value (for the jth profile)
$\overline{V}_{(j)}$	Counts	Simulated radiometric value (for the jth profile)
$\hat{V}$	Counts	Actual radiometric value
ε_V	—	Shading error for radiometric quantity V
ε_{E_d}	—	Shading error for downwelling irradiance
ε_{L_u}	—	Shading error for upwelling radiance
θ_0	Deg	Sun zenith angle
ϕ_0	Deg	Sun azimuth angle (measured clockwise with respect to the local north)

APPENDIX B

Acronyms

AAOT	Acqua Alta Oceanographic Tower
A/D	Analog-to-Digital
ADF	Angular Distribution Function
CEC	Commission of the European Communities
FOV	Field of View
GSFC	Goddard Space Flight Center

IC	Imperial College of Science, Technology and Medicine
IOP	Inherent Optical Property
JRC	Joint Research Centre
LoCNESS	Low Cost NASA Environmental Sampling System
MC	Monte Carlo
MVDS	Multichannel Visible Detector System
NASA	National Aeronautics and Space Administration
PHO-TRAN	Photon-Transport code
RSMAS	Rosenstiel School for Marine and Atmospheric Science
RTE	Radiative Transfer Equation
SeaOPS	SeaWiFS Optical Profiling System
SeaWiFS	Sea-viewing Wide Field-of-view Sensor
S/N	Serial Number
3D	Three-dimensional
WiSPER	Wire-Stabilized Profiling Environmental Radiometer

REFERENCES

Ångström, A., 1961: Techniques of determining the turbidity of the atmosphere. *Tellus,* **13,** 214–223.

Case, K. M., 1957: Transfer problems and the reciprocity principle. *Rev. Mod. Phys.,* **29,** 651–663.

Degobbis, D., S. Fonda-Umani, P. Franco, A. Malej, R. Precali, and N. Smodlaka, 1995: Changes in the northern Adriatic ecosystem and the hypertrophic appearance of gelatinous aggregates. *Sci. Total Environ.,* **165,** 43–58.

Doyle, J. P., and H. Rief, 1998: Photon transport in 3D structures treated by random walk techniques: Monte Carlo benchmark of ocean color simulations. *Math. Comput. Simul.,* **47,** 215–241.

Elterman, L., 1968: UV, visible, and IR attenuation for altitudes to 50 km. Rep. AFCRL-68-0153, U.S. Air Force Cambridge Research Laboratory, Bedford, MA, 56 pp.

Frölich, C., and G.E. Shaw, 1980: New determination of Rayleigh scattering in the terrestrial atmosphere. *Appl. Opt.,* **19,** 1773–1775.

Gordon, H. R., 1985: Ship perturbation of irradiance measurements at sea. Part 1: Monte Carlo simulations. *Appl. Opt.,* **24,** 4172–4182.

——, and D. J. Castaño, 1987: The Coastal Zone Color Scanner atmospheric correction algorithm: Multiple scattering effects. *Appl. Opt.,* **26,** 2111–2122.

——, and K. Ding, 1992: Self-shading of in-water optical instruments. *Limnol. Oceanogr.,* **37,** 491–500.

——, O. B. Brown, and M. M. Jacobs, 1975: Computed relationships between the inherent and apparent optical properties of a flat homogeneous ocean. *Appl. Opt.,* **14,** 417–427.

Helliwell, W. S., G. N. Sullivan, B. Macdonald, and K. J. Voss, 1990: Ship shadowing: Model and data comparison. *Proc. Ocean Optics X,* Orlando, FL, SPIE, 55–71.

Hooker, S. B., and W. E. Esaias, 1993: An overview of the SeaWiFS project. *Eos, Trans. Amer. Geophys. Union,* **74,** 241–246.

——, and C. R. McClain, 1999: A comprehensive plan for the calibration and validation of SeaWiFS data. *Progress in Oceanography,* Pergamon Press, in press.

Kearns, E., R. Riley, and C. Woody, 1996: A bio-optical time series collected in coastal waters for SeaWiFS calibration and validation: Large structure shadowing considerations. *Proc. Ocean Optics XIII,* Halifax, NS, Canada, SPIE 2963, 697–702.

Kirk, J. T. O., 1994: Estimation of the absorption and the scattering coefficients of natural waters by use of underwater irradiance measurements. *Appl. Opt.,* **33,** 3276–3278.

Leckner, B., 1978: The spectral distribution of solar radiation at the Earth's surface—Elements of a model. *Sol. Energy,* **20,** 143–150.

Lux, I., and L. Koblinger, 1991: *Monte Carlo Transport Methods; Neutron and Photon Calculations.* CRC Press, 517 pp.

Molin, D., E. Guidoboni, and A. Lodovisi, 1992: Mucilage and the phenomena of algae in the history of the Adriatic: Periodization and the antrophic context (17th–20th centuries). *Proc. of the International Conf. Marine Coastal Eutrophication,* R. Avollenweider, R. Marchetti, and R. Viviani, Eds., Elsevier, 511–524.

Mueller, J. L., and R. W. Austin, 1995: Ocean optics protocols for SeaWiFS validation, Revision 1. NASA Tech. Memo. 104566, Vol. 25, S. B. Hooker, E. R. Firestone, and J. G. Acker, Eds., NASA/Goddard Space Flight Center, Greenbelt, MD, 66 pp.

Robinson, N., 1966: *Solar Radiation.* Elsevier, 347 pp.

Saruya, Y., T. Oishi, M. Kishino, Y. Jodai, K. Kadokura, and A. Tanaka, 1996: Influence of ship shadow on underwater iradiance fields. *Proc. Ocean Optics XIII,* Halifax, NS, Canada, SPIE 2963, 760–765.

Spanier, J., and E. M. Gelbard, 1969: *Monte Carlo Principles and Neutron Transport Problems.* Addison-Wesley, 234 pp.

Vigroux, E., 1953: Contribution à l'étude expérimentale de l'absorption de l'ozone. *Ann. Phys.,* **8,** 709–762.

Voss, K. J., J. W. Nolten, and G. D. Edwards, 1986: Ship shadow effects on apparent optical properties. *Proc. Ocean Optics VIII,* Orlando, FL, SPIE, 186–190.

Weir, C. T., D. A. Siegel, A. F. Michaels, and D. W. Menzies, 1994: In situ evaluation of a ship's shadow. *Proc. Ocean Optics XII,* Bergen, Norway, SPIE 2258, 815–821.

Young, A. T., 1980: Revised depolarization corrections for atmospheric extinction. *Appl. Opt.,* **19,** 3427–3428.

Zibordi, G., and M. Ferrari, 1995: Instrument self-shading in underwater optical measurements: Experimental data. *Appl. Opt.,* **34,** 2750–2754.

——, V. Barale, G. M. Ferrari, N. Hoepffner, L. Alberotanza, P. Cova, and C. Ramasco, 1995: Coastal Atmosphere and Sea Time-Series project (CoASTS): An ocean color remote sensing calibration–validation project. *Proc. Third Thematic Conf. Remote Sensing for Marine and Coastal Environments,* Vol. II, 96–100.